Supplementary Materials

MXene interlayer–confined $CuFeO_2$ electroactive membrane for efficient activation of peroxymonosulfate and continuous-flow degradation of 17α-ethynylestradiol

Changjiang He[1,#], Meng Li[2,#], Xiaowei Ran[1], Yanbiao Liu[3,*], Fengzhi Jiang[1,2,*]

[1]School of Chemical Science and Technology, Yunnan University, Kunming 650091, Yunnan, China.
[2]Institute of International Rivers and Eco-Security, Yunnan University, Kunming 650091, Yunnan, China.
[3]School of Environmental Science and Technology, Key Laboratory of Industrial Ecology and Environmental Engineering (Ministry of Education), Dalian University of Technology, Dalian 116024, Liaoning, China.
[#]These authors contributed equally to this work.

[*]**Correspondence to:** Prof. Fengzhi Jiang, School of Chemical Science and Technology, Yunnan University, Kunming 650091, Yunnan, China. E-mail: fengzhij@ynu.edu.cn; Prof. Yanbiao Liu, School of Environmental Science and Technology, Key Laboratory of Industrial Ecology and Environmental Engineering (Ministry of Education), Dalian University of Technology, Dalian 116024, Liaoning, China.E-mail: yanbiaoliu@dlut.edu.cn

Contents

1. Experimental Section

1.1 Chemical Reagents

1.2 Experimental Instruments and Characterization Methods

1.3 Solution Preparation

1.3.1 Preparation of Potassium Ferricyanide Solution

1.3.2 Preparation of Actual Water Samples

1.4 Membrane Performance-Related Calculations (Flux J, Porosity ε, Equivalent Residence Time τ)

1.5 Degradation Product Analysis and Toxicity Assessment (Fukui indices, LC–MS, T.E.S.T.)

1.6 Theoretical Calculation Methods

2. Supplementary Tables and Figures

Supplementary Figures:

Supplementary Figure 1. Schematic diagram of the reactor structure

Supplementary Figure 2. EDS spectrum of MXene

Supplementary Figure 3. EDS spectrum of $CuFeO_2$–MX

Supplementary Figure 4. N_2 adsorption–desorption isotherms and pore size distribution of MXene, $CuFeO_2$, and $CuFeO_2$–MX

Supplementary Figure 5. XPS survey spectrum and high-resolution spectra (O 1s, C 1s, Fe 2p, Cu 2p) for $CuFeO_2$

Supplementary Figure 6. Comparison of catalytic performance of $CuFeO_2$–MX and physically mixed $CuFeO_2$/MX

Supplementary Figure 7. Comparison of EE2 removal under continuous-flow and static batch conditions

Supplementary Figure 8. Nyquist plots (EIS) of MXene, $CuFeO_2$, and $CuFeO_2$–MX

Supplementary Figure 9. I–t curves of MXene, $CuFeO_2$, and $CuFeO_2$–MX

Supplementary Figure 10. SEM image of $CuFeO_2$–MX after 400 min of continuous treatment

Supplementary Figure 11. BET results of $CuFeO_2$–MX after 400 min of continuous treatment

Supplementary Figure 12. Fukui (f^0) function isosurface map of EE2

Supplementary Figure 13. LC–MS identification of degradation intermediates
Supplementary Figure 14. Comparison of bioaccumulation factors between intermediates and EE2
Supplementary Figure 15. Comparison of developmental toxicity between intermediates and EE2
Supplementary Figure 16. TDOS and PDOS of $CuFeO_2$–MX and MX–$CuFeO_2$–MX
Supplementary Figure 17. Adsorption configurations and energies of PMS on different substrates/interfaces
Supplementary Figure 18. Adsorption configurations and energies of EE2 on different substrates/interfaces

Supplementary Tables:

Supplementary Table 1. Water quality parameters of Dianchi Lake used in this study
Supplementary Table 2. ICP-OES analysis of Cu and Fe leaching from $CuFeO_2$–MX membrane after electrochemical operation
Supplementary Table 3. f^0 values of each atom in EE2
Supplementary Table 4. Bader charge analysis of $CuFeO_2$–MX and MX–$CuFeO_2$–MX

1. Experimental Section

1.1 Chemical Reagents

The main chemical reagents used in this study were as follows: Ti_3AlC_2 MAX phase powder, hydrofluoric acid (HF, 50%), tert-butanol (TBA), potassium ferricyanide ($K_3[Fe(CN)_6]$), copper nitrate trihydrate ($Cu(NO_3)_2 \cdot 3H_2O$), and iron nitrate nonahydrate ($Fe(NO_3)_3 \cdot 9H_2O$) were purchased from Shanghai Adamas Reagent Co., Ltd. p-Benzoquinone (p-BQ) and L-histidine (L-His) were obtained from Shanghai Aladdin Biochemical Technology Co., Ltd. Disodium ethylenediaminetetraacetate (EDTA-2Na), sodium chloride (NaCl), sodium sulfate (Na_2SO_4), sodium carbonate (Na_2CO_3), sodium nitrate ($NaNO_3$), and sodium hydroxide (NaOH) were purchased from Tianjin Zhiyuan Chemical Reagent Co., Ltd.17α-Ethinylestradiol (EE2, ≥98%) was purchased from Sigma-Aldrich (Shanghai) Trading Co., Ltd. Methanol and acetonitrile (HPLC grade) were obtained from Tedia Company. Peroxymonosulfate (PMS, calculated as $KHSO_5 \cdot 0.5KHSO_4 \cdot 0.5K_2SO_4$) was purchased from Shanghai Macklin Biochemical Technology Co., Ltd.All chemicals were used as received without further purification. Ultrapure water (18.2 MΩ·cm) was used throughout the experiments.

1.2 Experimental Instruments

The main instruments used in this study included a Rigaku SmartLab 600 X-ray diffractometer, a ZEISS GeminiSEM 300 scanning electron microscope equipped with an energy-dispersive spectroscopy (EDS) system, a Thermo Scientific K-Alpha X-ray photoelectron spectrometer, a Micromeritics ASAP 2460 physical adsorption analyzer, a Thermo Fisher Scientific Nicolet iS20 Fourier transform infrared spectrometer, a Bruker EMXplus-6/1 electron paramagnetic resonance spectrometer, and an Agilent 1260 Infinity II high-performance liquid chromatograph.

The crystal structures of the samples were analyzed using X-ray diffraction (XRD) with Cu Kα radiation (λ = 1.5406 Å). The morphology and elemental distribution of the samples were observed using scanning electron microscopy (SEM) coupled with energy-dispersive X-ray spectroscopy (EDS). The surface chemical states of the elements were analyzed using X-ray photoelectron spectroscopy (XPS) with an Al Kα excitation source, and the binding energies were calibrated using the C 1s peak at 284.8 eV. Nitrogen adsorption–desorption isotherms were measured at 77 K using a physical adsorption analyzer, and the specific surface area was calculated using the Brunauer–Emmett–Teller (BET) model. Functional groups were analyzed using

Fourier transform infrared spectroscopy (FT-IR) in the wavenumber range of 400–4000 cm^{-1}. Reactive oxygen species generated during the reaction were identified by electron paramagnetic resonance (EPR) using DMPO (for ·OH and $\cdot SO_4^-$) and TEMP (for $^1O_2$) as spin-trapping agents.Electrochemical measurements were carried out using a CHI 760E electrochemical workstation in a three-electrode system. Electrochemical impedance spectroscopy (EIS) (frequency range 0.1 Hz–100 kHz, amplitude 10 mV) and chronoamperometry (I–t) tests were conducted in an electrolyte containing 5 mM $K_3[Fe(CN)_6]$ and 0.1 M KCl.

1.3 Solution Preparation

1.3.1 Preparation of Potassium Ferricyanide Solution

Accurately weigh 0.4115 g of $K_3[Fe(CN)_6]$ and 1.8638 g of KCl, dissolve them in ultrapure water, and transfer the solution into a 250 mL volumetric flask. Dilute to the mark with ultrapure water to obtain a mixed solution containing 5 mM $K_3[Fe(CN)_6]$ and 0.100 M KCl.

1.3.2 Preparation of Actual Water Samples

To verify the applicability of the proposed method for real water samples, water was collected from Dianchi Lake at Laoyu River Wetland Park in Kunming. The samples were filtered through a 0.45 μm membrane filter to remove suspended particles such as sediment. The filtered water was then spiked with EE2 to a concentration of 3 $mg \cdot L^{-1}$ for subsequent experiments.

1.4 Membrane Performance-Related Calculations

Permeation flux (J) was calculated according to Eq. (1):

$$J=\frac{V_t}{A_m T}\ \left(L/(m^2 h^1)\right) \tag{1}$$

where J is the permeation flux ($L \cdot m^{-2} \cdot h^{-1}$), V_t is the permeate volume (L), A_m is the effective membrane area (m^2), and T is the filtration time (h).

Membrane porosity (ε):

The porosity was determined using the gravimetric method [20]. The dry membrane was first weighed to obtain W_1, then completely immersed in anhydrous ethanol for 0.5 h. After removal, the surface liquid was quickly wiped off with filter paper and the membrane was weighed again to obtain W_2. The membrane porosity was calculated using Eq. (2):

$$\varepsilon=\frac{W_2-W_1}{A_m \sigma \rho}=\frac{W_2-W_1}{\rho}\times\frac{1}{A_m \sigma}=\frac{\text{pore volume}}{\text{Membrane volume}} \tag{2}$$

where σ is the membrane thickness (m) and ρ is the density of ethanol ($g \cdot cm^{-3}$). The calculated porosity of the membrane used in this study was approximately 70.40%.

Hydraulic residence time (τ) was estimated according to Eq. (3):

$$\tau_m = \frac{V_m W}{J A_m} = \frac{\varepsilon \sigma}{J} \quad (3)$$

where W is the membrane weight and V_m is the specific pore volume (pore volume per unit membrane weight) .

1.5 Degradation Product Analysis and Toxicity Assessment

The Fukui function, based on density functional theory (DFT), was employed to predict the radical reaction activity of each atom in the EE2 molecule. All calculations were performed using the ORCA software package. Specifically, the Fukui function can be classified into three types:

f^+: describes electrophilic reactivity, representing the ability of a molecule to accept electrons.

f^-: describes nucleophilic reactivity, representing the ability of a molecule to donate electrons.

f^0: describes radical reactivity, indicating the ability of a molecule to both accept and donate electrons.

The isosurface map of the f^0 function was analyzed to determine the sites most susceptible to radical attack.

The degradation intermediates were identified using liquid chromatography–mass spectrometry (LC–MS, Thermo Scientific LTQ Orbitrap XL). Based on the identified intermediate structures, the Toxicity Estimation Software Tool (T.E.S.T.) developed by the U.S. Environmental Protection Agency (EPA) was employed to predict the bioaccumulation factor and developmental toxicity of the degradation products.

1.6 Theoretical Calculation Methods

All first-principles calculations in this study were performed using the Vienna Ab initio Simulation Package (VASP). The interaction between ionic cores and valence electrons was described using the projector augmented-wave (PAW) method. The Perdew–Burke–Ernzerhof (PBE) functional within the generalized gradient approximation (GGA) was employed to describe the exchange–correlation interaction, and Grimme's DFT-D3 method was introduced to account for van der Waals interactions.

The plane-wave cutoff energy was set to 450 eV. For structural optimization and

property calculations, the Brillouin zone integration was performed using a 1 × 1 × 1 Monkhorst–Pack k-point grid. The convergence criterion for the self-consistent field (SCF) calculations was set to 10^{-5} eV, and the maximum residual force on each atom was converged to 0.02 eV·Å^{-1}.

The adsorption energy (E_ads) was calculated using the following equation:

$$E_{ads} = E_{total} - E_{substrate} - E_{adsorbate} \quad (3)$$

where E_total, E_substrate, and E_adsorbate represent the total energies of the adsorption system, the substrate, and the adsorbate, respectively.

The climbing image nudged elastic band (CI-NEB) method was used to determine the reaction transition states and energy barriers.

2. Supplementary Tables and Figures

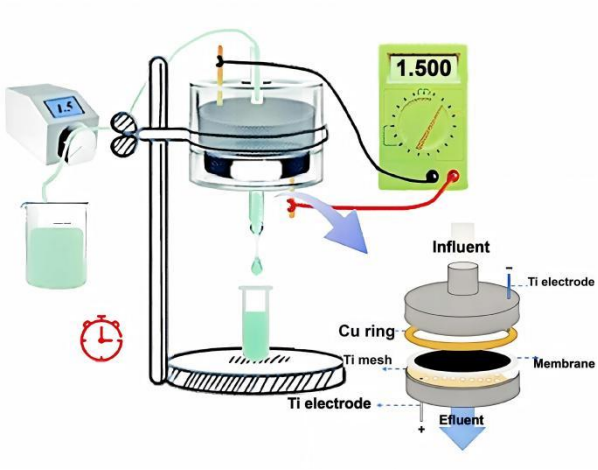

Supplementary Figure 1. Schematic diagram of the reactor structure.

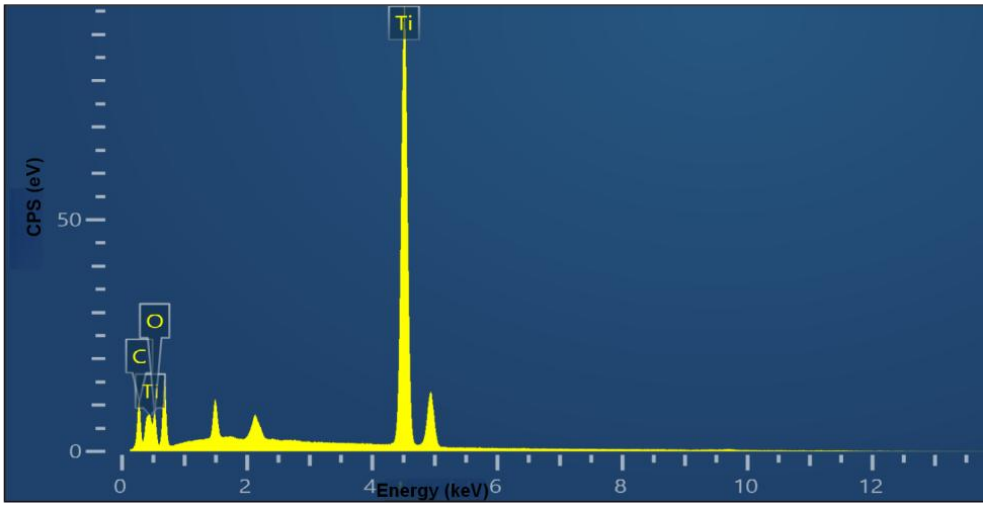

Supplementary Figure 2. EDS spectrum of MXene.

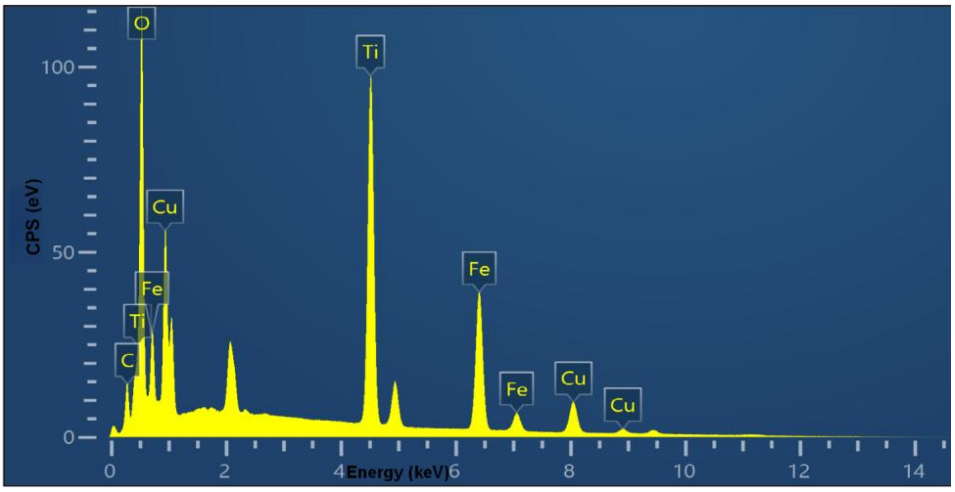

Supplementary Figure 3. EDS spectrum of $CuFeO_2$–MX.

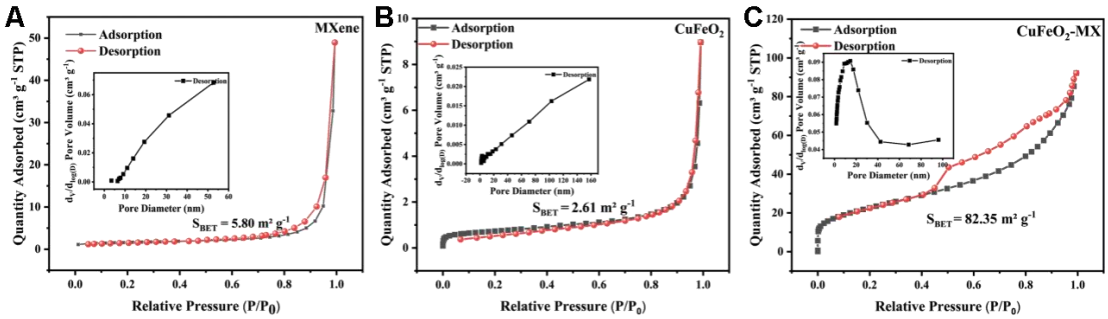

Supplementary Figure 4. N_2 adsorption–desorption isotherms and pore size distribution of (A) MXene, (B) $CuFeO_2$, and (C) $CuFeO_2$–MX.

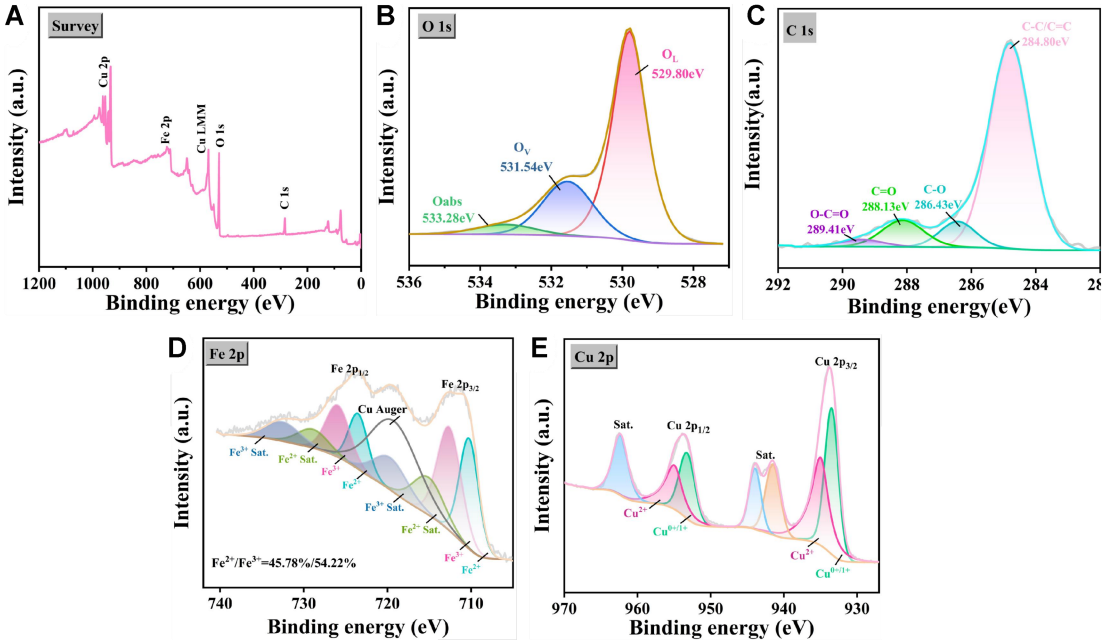

Supplementary Figure 5. XPS survey spectrum (A) and O 1s (B), C 1s (C), Fe 2p (D), and Cu 2p (E) high-resolution spectra for $CuFeO_2$.

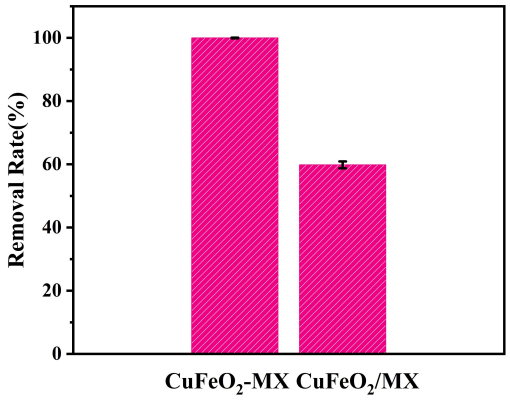

Supplementary Figure 6. Comparison of the catalytic performance of $CuFeO_2$–MX and physically mixed $CuFeO_2$/MX samples.Data are presented as mean ± standard deviation (SD) (n=3).

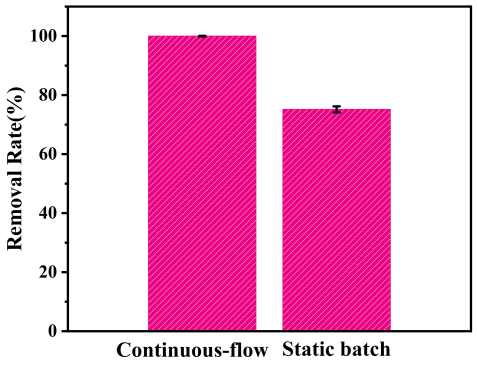

Supplementary Figure 7. Comparison of EE2 removal performance under continuous-flow and static batch conditions.Data are presented as mean ± standard deviation (SD) (n=3).

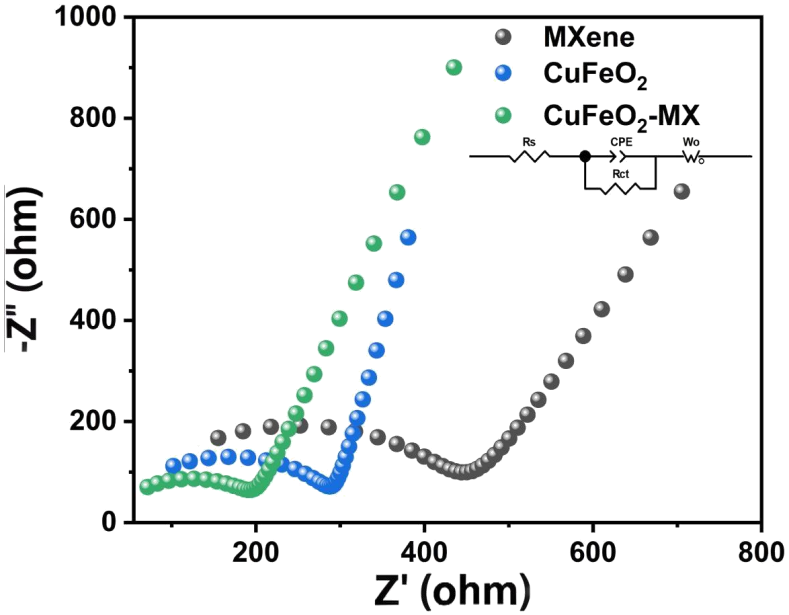

Supplementary Figure 8. Nyquist plots (EIS) of MXene, $CuFeO_2$, and $CuFeO_2$–MX.

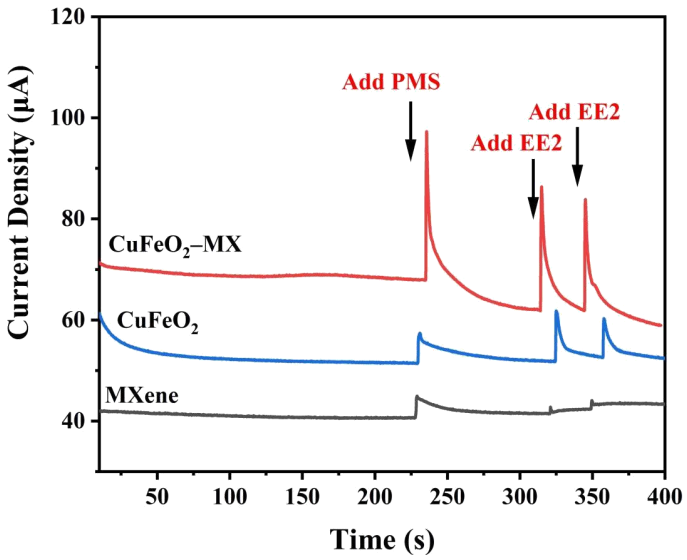

Supplementary Figure 9. I–t curve of the MXene, $CuFeO_2$, and $CuFeO_2$–MX.

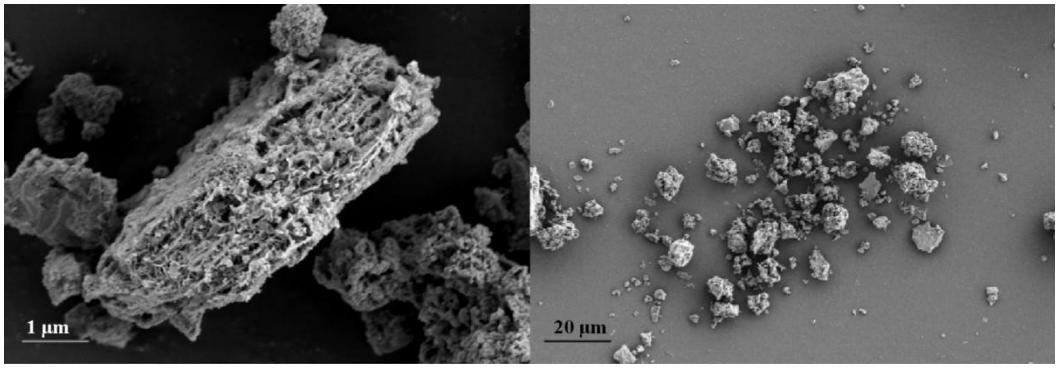

Supplementary Figure 10. SEM image of $CuFeO_2$–MX after 400 min of continuous treatment.

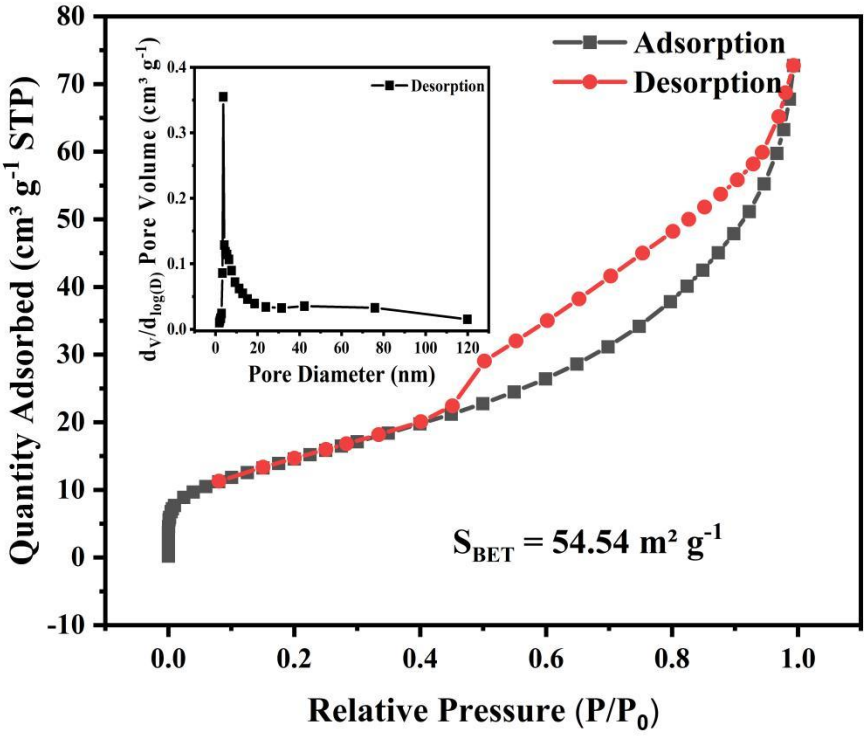

Supplementary Figure 11. BET results of $CuFeO_2$–MX after 400 min of continuous treatment.

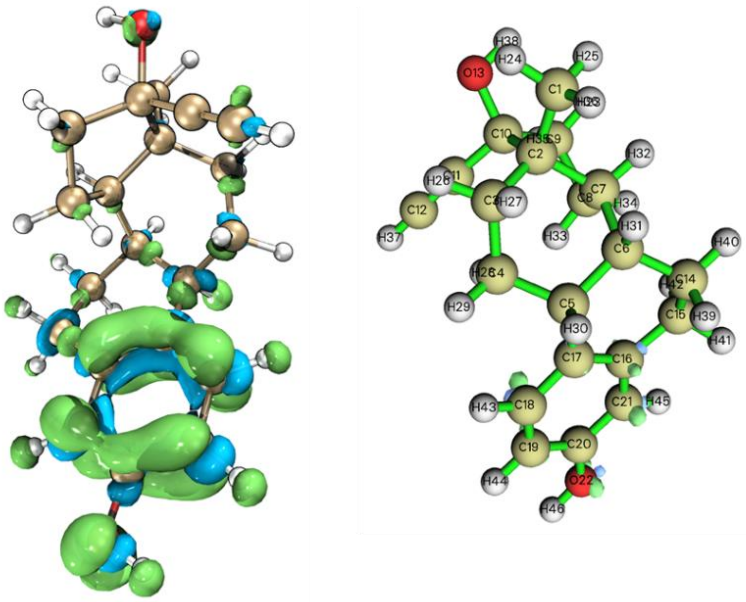

Supplementary Figure 12. Fukui (f^0) function isosurface map of EE2.

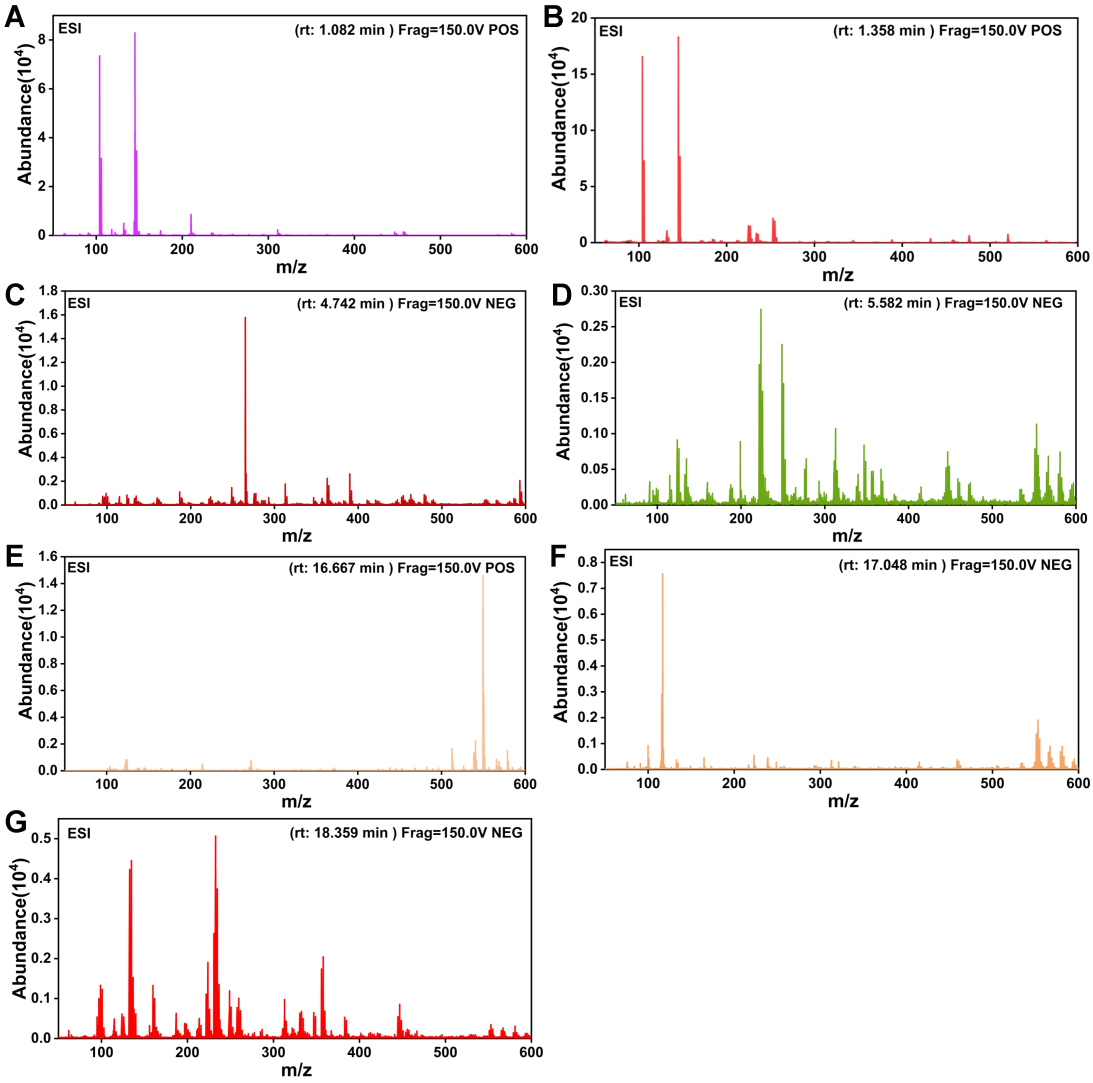

Supplementary Figure 13. LC–MS identification of degradation intermediates. (A and B) positive ion mode; (C-G) negative ion mode. Fragmentor voltage: 150.0 V; retention times are marked in each sub-graph.

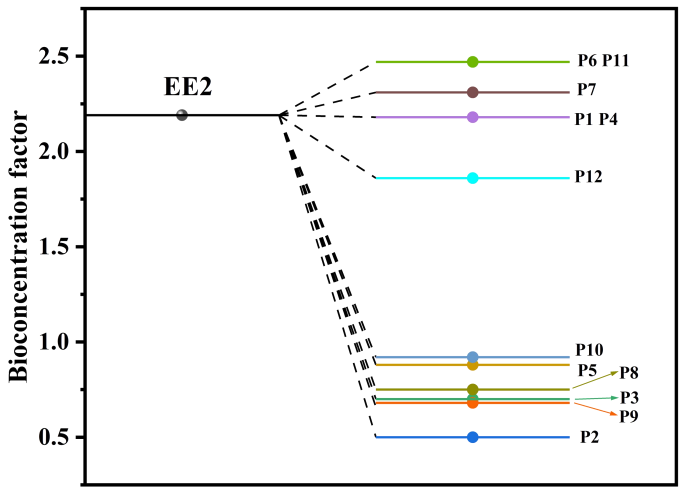

Supplementary Figure 14. Comparison of bioaccumulation factors between intermediates and EE2.

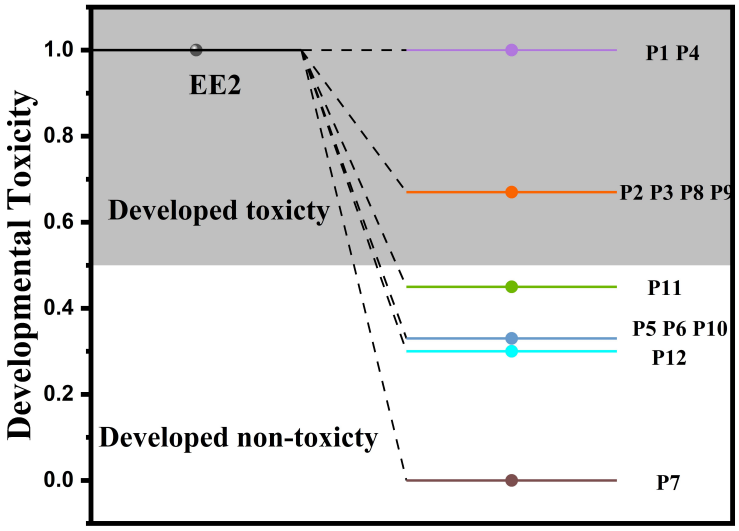

Supplementary Figure 15. Comparison of developmental toxicity between intermediates and EE2.

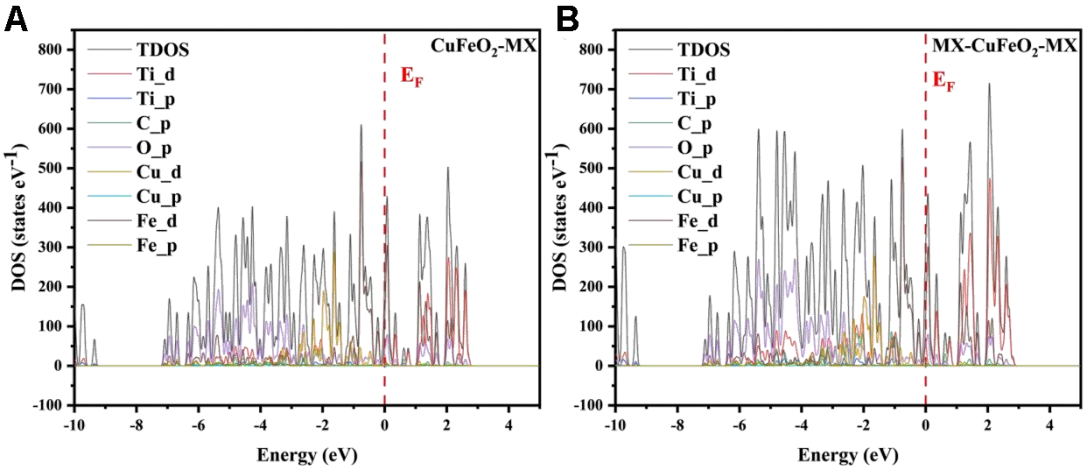

Supplementary Figure 16. TDOS and PDOS of $CuFeO_2$–MX (A) and MX–$CuFeO_2$–MX (B).

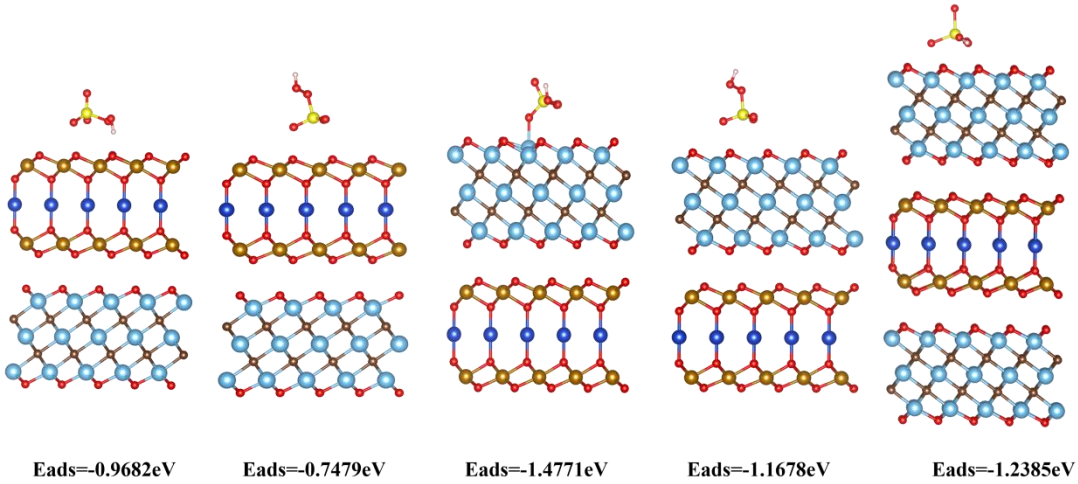

Supplementary Figure 17. Adsorption configurations and adsorption energies of PMS on different substrates/interfaces.

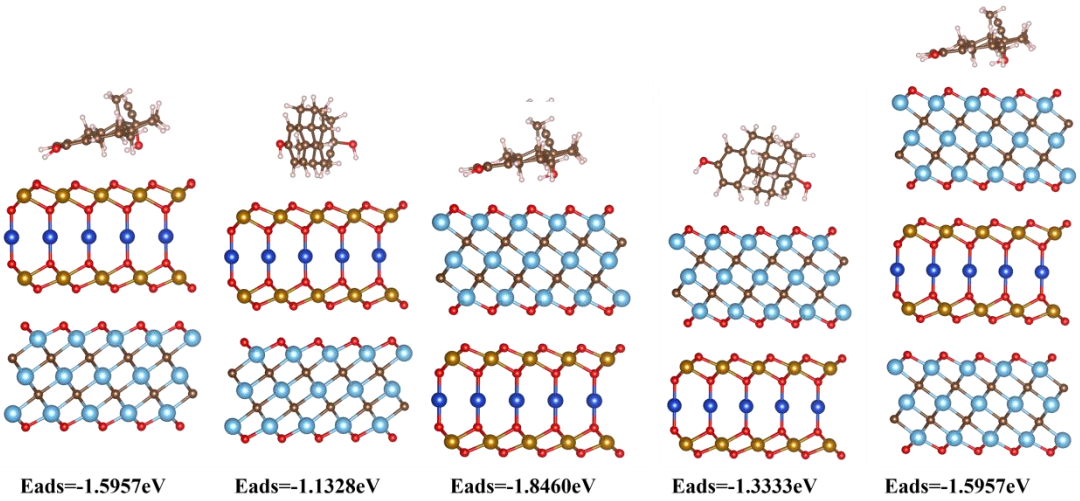

Supplementary Figure 18. Adsorption configurations and adsorption energies of EE2 on different substrates/interfaces.

Supplementary Table 1. Water quality parameters of Dianchi Lake used in this study

Parameter	Dianchi Lake
COD (mg L^{-1})	12.3
pH	7.57
TOC (mg L^{-1})	1.69
HCO_3^- (mg L^{-1})	130
Ca (mg L^{-1})	39.6
K (mg L^{-1})	6.16
Mg (mg L^{-1})	9.32
Na (mg L^{-1})	14.8
Total hardness (mg L^{-1})	130
DO (mg L^{-1})	5.63
Color (°)	<2.9
Conductivity (μS cm^{-1})	321

Supplementary Table 2. ICP-OES analysis of Cu and Fe leaching from $CuFeO_2$–MX membrane after electrochemical operation

Metal ions	Concentration (mg L^{-1})	RSD(%)
Cu	0.7194 mg/L	3.71
Fe	0.02270 mg/L	5.39

Supplementary Table 3. f^0 values of each atom in EE2

Atom	q(N)	q(N+1)	q(N-1)	f^0
1(C)	-0.089	-0.0963	-0.0834	0.0065
2(C)	0.0124	0.0115	0.0163	0.0024
3(C)	-0.0528	-0.0585	-0.044	0.0072
4(C)	-0.055	-0.0589	-0.0463	0.0063
5(C)	-0.0163	-0.0206	-0.0026	0.009
6(C)	-0.0177	-0.0204	-0.0123	0.0041
7(C)	-0.0203	-0.0193	-0.018	0.0006
8(C)	-0.0553	-0.056	-0.0537	0.0012
9(C)	-0.0541	-0.0617	-0.044	0.0088
10(C)	0.0996	0.0915	1.0151	0.0068
11(C)	-0.0324	-0.0576	-0.0251	0.0162
12(C)	-0.1036	-0.151	-0.0739	0.0385
13(O)	-0.2251	-0.2486	-0.1953	0.0267
14(C)	-0.0485	-0.0561	-0.0419	0.0071
15(C)	-0.0477	-0.0642	-0.0377	0.0133
16(C)	-0.0001	-0.0608	0.0434	0.0521
17(C)	-0.0152	-0.0441	0.0729	0.0585
18(C)	-0.0455	-0.1417	0.0032	0.0725
19(C)	-0.0783	-0.1591	-0.0165	0.0713
20(C)	0.0681	0.0307	0.1434	0.0564
21(C)	-0.0682	-0.1593	-0.0153	0.072
22(O)	-0.1974	-0.2313	-0.0968	0.0672
23(H)	0.0297	0.021	0.0365	0.0078
24(H)	0.0319	0.0214	0.0426	0.0106
25(H)	0.0224	0.011	0.0317	0.0104
26(H)	0.0297	0.019	0.0451	0.0131
27(H)	0.024	0.0124	0.035	0.0113
28(H)	0.0186	0.0176	0.0221	0.0023
29(H)	0.027	0.0171	0.0392	0.011
30(H)	0.0266	0.009	0.0622	0.0266
31(H)	0.025	0.0097	0.0401	0.0152

Atom	q(N)	q(N+1)	q(N-1)	f^0
32(H)	0.0211	0.0113	0.034	0.0114
33(H)	0.0304	0.0368	0.0237	-0.0066
34(H)	0.0301	0.0253	0.0354	0.0051
35(H)	0.0368	0.0265	0.0478	0.0107
36(H)	0.0272	0.014	0.0392	0.0126
37(H)	0.0925	0.0729	0.1051	0.0161
38(H)	0.154	0.1237	0.1657	0.021
39(H)	0.0279	0.0166	0.0381	0.0108
40(H)	0.0272	0.0071	0.0472	0.0201
41(H)	0.033	0.0073	0.0525	0.0226
42(H)	0.0304	0.0051	0.0482	0.0216
43(H)	0.0402	-0.0018	0.0698	0.0358

Supplementary Table 4. Bader charge analysis of $CuFeO_2$–MX and MX–$CuFeO_2$–MX

	Bader(e)
$CuFeO_2$–MX	**2.21563**
MX–$CuFeO_2$–MX	**4.05821**